Non-invasive multilevel geometric regularization of mesh-based 3D shape measurement

Guillaume Colantonio, Morgane Chapelier, Robin Bouclier, Jean-Charles Passieux, Eduard Marenić

Received: Added at production | Revised: Added at production | Accepted: Added at production

DOI: 10.1002/nme.6291

ARTICLE TYPE

Non-invasive multilevel geometric regularization of mesh-based 3D shape measurement

Guillaume Colantonio[1] | Morgane Chapelier[1,2] | Robin Bouclier[1,2] | Jean-Charles Passieux*[1] | Eduard Marenić[1]

[1]Institut Clement Ader (ICA), Université de Toulouse, CNRS-INSA-UPS-ISAE-Mines Albi, Toulouse, France
[2]Institut de Mathématiques de Toulouse (IMT), Université de Toulouse, CNRS-INSA-UT1-UT2-UP, Toulouse, France

Correspondence
*J.C. Passieux Email: passieux@insa-toulouse.fr

Present Address
135 avenue de Rangueil, 31077 Toulouse, Fr.

Summary

Finite element stereo digital image correlation (FE-SDIC) requires a crucial calibration phase in which the initial CAD needs to be updated to fit the actual shape of the specimen. On the one hand, the use of a FE mesh facilitates the coupling of measurements with simulation tools. On the other hand, it provides a unique, fine description of both the geometry and the displacement, which often makes the shape measurement problem highly ill-posed. As a remedy, we propose a hybrid isogeometric-FE strategy that can measure a shape in terms of spline functions while considering as an input and output the analysis-suitable FE mesh. Making use of the appealing spline refinement procedures and of Bézier-based operators, multilevel smooth spline discretizations are built concurrently with the initial FE subspace and related to the multi-scale images used for the initialization of the shape measurement. It results in a geometrically sound regularization which provides a spline parametrization of the optimal shape along with its FE twin. A non-invasive implementation from an existing FE-SDIC code is also detailed. The performance of the proposed method is assessed on real images and comparisons are made with other published techniques to prove its efficiency.

KEYWORDS:
Stereo-correlation, Finite elements, Free-form surfaces, NURBS, Multilevel design, Bézier extraction

1 | INTRODUCTION

The expanding use of finite elements (FE) meshes in digital image correlation (DIC) algorithms [1,2,3,4,5,6,7,8,9,10] is explained by their ability to be coupled with numerical models. The interaction of measurement and simulation becomes fast and friendly, as both kinematic fields are defined at the nodes of the same mesh. This potent framework paves the way to a better integration of models and experiments in solid mechanics [11,12,13,14,15].

When the specimen geometry or mechanical loading is not planar, a stereo digital image correlation (SDIC) method is used concurrently with, at least, two cameras, to access the three components of the displacement at the surface of the specimen. This method, initially developed in the context of subset-DIC [16,17], was recently extended to the context of global approaches [11,18,13]. For instance, global SDIC was successfully used for the analysis of complex experiments such as structural tests [19,14,20]. Before estimating the displacement measurement, SDIC requires a calibration phase aiming at determining the parameters of the cameras and the actual shape of the specimen. In FE simulations (and thus in FE-SDIC), a unique interpolation subspace is generally

used for both the approximation of the geometry and of the displacement (basic principle of isoparametric finite elements). The approximation subspace is therefore entirely defined by the choice of a FE mesh.

However, the shape of the specimen is generally rather smooth and regular and it should require less degrees of freedom than the displacement field which may comprise important gradients. Another way of considering FE-SDIC would consist in a suitable mix of an appropriate mesh for shape measurement and a different finer FE mesh that properly compute the displacement (*i.e.*, an analysis-suitable mesh). Using standard finite elements, such an approach would require non-trivial projection procedures between unstructured 3D surface meshes, which are often accompanied with a modification of the (generally curved) geometry.

To resolve this issue, the common practice consists in using a refined analysis-suitable FE mesh for both shape and displacement measurements, which could make the shape measurement problem highly ill-posed. As a result, regularization techniques based on the addition of specific terms [19,13] are often used to avoid getting wiggly, irregular shapes. Such regularization is also employed in a multi-scale initialization phase which consists in decreasingly filtering the images and modifying the size of the apparent approximation subspace by acting on the regularization level (*i.e.*, modifying the weight of the additional regularizing terms).

From a mathematical and a numerical point of view, we notice that the mesh-based shape measurement problem coming from the experimental mechanics community shares many similarities with the shape optimization problem encountered in structural design. Indeed, structural shape optimization also aims at finding the optimal geometry of a structure and involves a FE mesh in the process [21,22]. The difference only lies in the desired objective which is related to the fulfillment of a certain structural behavior in shape optimization while it concerns the fitting with the real surface in shape measurement. Therefore, the purpose of this work is to draw inspiration from the techniques developed in the area of shape optimization to improve the field of mesh-based shape measurement.

One approach in shape optimization is actually very close to what is performed for shape measurement: it consists in using the spatial location of the FE nodes as the design variables in combination with delicate mesh regularization techniques to prevent the appearance of irregular, "unrealistic" shapes [23,24]. Meanwhile, another class of techniques, denoted by the computer-aided-design (CAD)-based approach, has also emerged for shape optimization: the idea is to resort to the same spline-based functions as in CAD software to describe the geometry [25,26,27]. The design variables are this time the spatial location of the control points of the spline entities, which enables to get a light and smooth parametrization of the geometry and of its update [28,29]. The difficulty in this second family of methods is then transferred to the connection of the (spline-based) geometric and (FE-based) analysis models [30,31]. To answer this issue, one way to naturally proceed is to use the isogeometric analysis (IGA) framework [32,33] which enables to discretize the structure with its intrinsic, spline-based, CAD geometric definition. Isogeometric (IG) shape optimization has thus been successfully applied to a wide range of applications (see [34,35,36,37,38] among others). More precisely, it is based on a multilevel design concept offered by the spline technology in which one can refine the geometry without altering its initial shape and regularity [39]. As a consequence, different refinement levels of the same spline-based geometry are considered to define both design and analysis spaces. The coarser level is dedicated to the parametrization of the shape to get "realistic" structures while the finer level defines the analysis model and is set to ensure good quality of the mechanical solution.

A first attempt in applying IGA to shape measurement has been recently performed in Dufour *et al.* [40,18,19]. In these pioneering works, the authors considered a higher-order B-spline (monolevel) parametrization of the surface (thereby acting on a geometrical object which is consistent with CAD) both for shape and displacement measurements. The authors also went towards the identification of mechanical models by comparing the measured IG displacement field with a computed one using a dedicated IG code [12]. However, besides the effort to implement spline functions in the SDIC framework, the problem is that the user ends up with an experimental displacement field that is expressed on a spline basis, whereas most simulation tools are based on finite elements. Splines clearly provide flexibility for shape and displacement measurements but make connection with most of today's numerical models more complex, which is the key advantage of global approaches in DIC.

In this paper, we build a hybrid IG-FE methodology for mesh-based shape measurement that draws up the best of each technology. On the one hand, we consider as an input and output the FE mesh that is fine enough to properly describe the underlying mechanics. In a second step, the FE mesh will thus be suitable for displacement measurement using stereo-correlation and this resulting kinematic field will be easily compared to a computed one obtained from existing, standard FE codes. On the other hand, we undertake to use the splines along with the IG multilevel design concept (performed in shape optimization) for the description of the geometry and of its update in the shape measurement process. The idea here is to couple the multilevel optimization process with the multi-scale initialization of shape measurement to get different approximation spaces which naturally follow, at each level, the resolution of the image. The regularization level is thus given by the refinement of the spline spaces which is chosen in accordance with the coarsening of the images (no more need of additional regularization terms). Since it is

based on functions coming from the geometric design community, the proposed regularization scheme has a strong geometrical meaning, that is why we refer to geometric regularization to characterize the technique.

The additional ingredient of our approach is to make use of a recently developed global bridge between IGA and FE analysis (FEA)[41] to be able to communicate between the different approximation subspaces for the geometry (multilevel spline-based parametrizations) and for the displacement (analysis-suitable FE mesh). Based on the original idea behind Bézier extraction[42] and on more recent Lagrange extraction[43], this global transformation goes from Lagrange polynomials to (possibly rational) spline basis, thus enabling to recover an IG operator without implementing IGA but simply by projecting an FE operator onto the reduced, more regular, IG basis. As a result, besides its attractive regularizing features, the implementation of the proposed strategy is non-invasive with respect to FE-SDIC.

The paper is organized as follows: after this introduction, Section 2 specifies the calibration phase occurring in FE-SDIC with a particular emphasis on the shape measurement problem. Then, Section 3 is devoted to the development of the proposed geometric regularization scheme while Section 4 assesses the performance of the methodology through the analysis of several real images and comparisons with other published techniques. This brings us to Section 5 where concluding remarks are drawn.

2 | MESH-BASED SHAPE MEASUREMENT

Let us assume that we have an existing description (say a CAD model) of the nominal geometry of the specimen, which, in experimental mechanics, is generally the case. Let Ω_s be a surface domain referred to as Region of Interest (ROI) and such that $\Omega_s \subset \mathbb{R}^3$ corresponds to the visible surface of the theoretical shape. This representation does not correspond exactly to the actual shape of the specimen, because of surface roughness, manufacturing defects, pre-load or relaxation of residual stresses, to name a few. In SDIC, the estimation of the real surface is of the utmost importance because it is an essential prerequisite for 3D surface displacement measurement. It may also be used to update the model geometry in validation and/or identification procedures, since kinematic fields may significantly depend on it.

2.1 | Camera model

As classically done in SDIC[44], each camera c is equipped with a camera model $\mathbf{P}_c$ that maps any 3D point $\mathbf{X} \in \Omega_s$ expressed in the world reference system $\mathcal{R}_w$ to the corresponding coordinates in pixels $\mathbf{x}_c$ in the image frame and is written as:

$$\mathbf{P}_c : \mathbb{R}^3 \to \mathbb{R}^2, \quad \mathbf{X} \mapsto \mathbf{x}_c = \mathbf{P}_c(\mathbf{X}, \mathbf{p}_c), \qquad \forall \mathbf{X} \in \Omega_s, \tag{1}$$

where $\mathbf{p}_c$ is a vector collecting the model's parameters. More precisely, camera models $\mathbf{P}_c$ can be either linear (in homogeneous coordinates) or non-linear to take into account lens distortions. It depends on two sets of parameters: the intrinsic parameters (focal length, image center, horizontal/vertical aspect ratio, skew and possible distortion parameters) and the extrinsic parameters (3 rotations and 3 translations that map the reference frame of the specimen $\mathcal{R}_w$ to that of the imaging sensor $\mathcal{R}_c$). The calibration of these parameters must be done prior to any measurement. In this study, intrinsic parameters are calibrated using calibration targets and a classic photogrammetric technique as described in[45,46]. In the remainder of this article, the instrinic parameters will be assumed to be known and only the extrinsic parameters will be considered, such that for each camera c, the camera model $\mathbf{P}_c$ will be entirely defined by $\mathbf{p}_c \in \mathbb{R}^6$.

2.2 | Coupled calibration and shape measurement problem

As depicted in Figure 1, the graylevel conservation assumption[47] supposes that the graylevel value $\mathcal{I}_c(\mathbf{x}_c)$ of the projections $\mathbf{x}_c$ in each image $\mathcal{I}_c$ of any 3D point $\mathbf{X}$ should be equal: $\mathcal{I}_0(\mathbf{x}_0) = \mathcal{I}_1(\mathbf{x}_1)$. Since both the actual shape and position of the specimen (with respect to the stereo rig) are not known exactly, the graylevel conservation is not fulfilled. The calibration of the stereo rig thus consists in a coupled problem aiming at finding the extrinsic parameters $\mathbf{p} = [\mathbf{p}_0, \mathbf{p}_1]$ in addition to a shape correction field $\mathbf{S}(\mathbf{X}), \forall \mathbf{X} \in \Omega_s$, such that the advection of the nominal surface Ω_s by the correction field $\mathbf{S}(\mathbf{X})$ corresponds to the actual surface. More precisely, shape correction and camera parameters minimize the graylevel mismatch:

$$\mathbf{S}^\star, \mathbf{p}^\star = \underset{\mathbf{S}\in L_2(\Omega_s), \mathbf{p}\in\mathbb{R}^{12}}{\arg\min} \; j(\mathbf{S}(\mathbf{X}), \mathbf{p}) \qquad \text{with} \qquad j(\mathbf{S}(\mathbf{X}), \mathbf{p}) = \frac{1}{2} \int_{\Omega_s} \Big(r\big(\mathbf{S}(\mathbf{X}), \mathbf{p}\big) \Big)^2 \, \mathrm{d}\mathbf{X}, \tag{2}$$

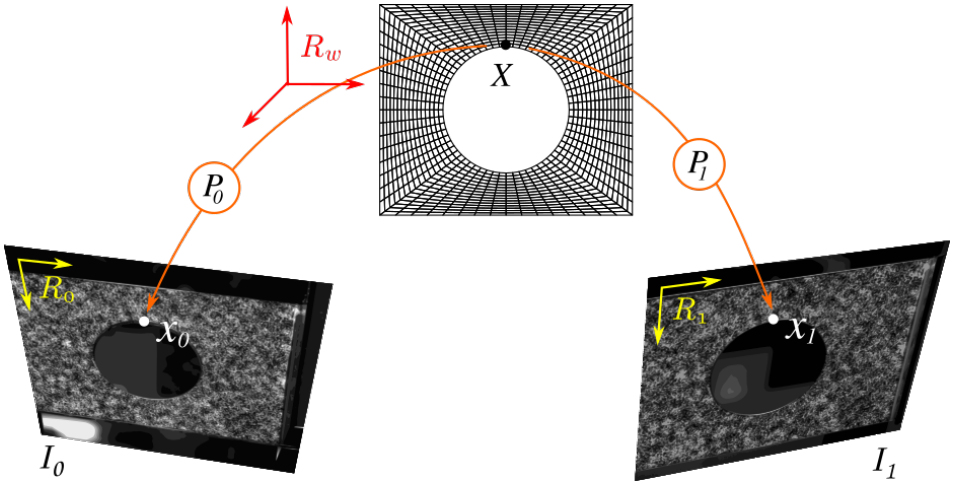

FIGURE 1 Principle of the formulation of the SDIC problem in the reference frame of the FE model. A 3D point $\mathbf{X}$ and its projections $\mathbf{x}_0$ and $\mathbf{x}_1$ onto the image planes.

and where the graylevel residual $r(\mathbf{S}(\mathbf{X}), \mathbf{p})$ is defined $\forall \mathbf{X} \in \Omega_s$ as:

$$r\big(\mathbf{S}(\mathbf{X}), \mathbf{p}\big) = \mathcal{I}_0\big(\mathbf{P}_0(\mathbf{X} + \mathbf{S}(\mathbf{X}), \mathbf{p}_0)\big) - \mathcal{I}_1\big(\mathbf{P}_1(\mathbf{X} + \mathbf{S}(\mathbf{X}), \mathbf{p}_1)\big). \tag{3}$$

Let us highlight, at this stage, that the graylevel residual is defined in Ω_s in the reference system of the model which differs from subset based SDIC, where it is written in the image frames.

The unknown vector $\mathbf{p}$ gathering the extrinsic parameters is already discrete, but the shape correction field $\mathbf{S}$ lies in an infinite space. To solve Problem (2) an approximation subspace for $\mathbf{S}$ must be defined. To be consistent with the description of the geometry and displacements in FE simulations, $\mathbf{S}$ is searched for in an analysis-suitable FE subspace [13]:

$$\mathbf{S}(\mathbf{X}) = \sum_{I=1}^{n_{FE}} L_I(\mathbf{X})\, \mathbf{q}_I = \mathbf{L}^T(\mathbf{X})\, \mathbf{q}, \tag{4}$$

where $\mathbf{L}$ is a $(3n_{FE} \times 3)$ matrix gathering the n_{FE} Lagrange shape functions L_I and $\mathbf{q}$ is a vector that collects the $3n_{FE}$ corresponding degrees of freedom (DOF):

$$\mathbf{L} = \begin{bmatrix} L_1 & 0 & 0 \\ \vdots & \vdots & \vdots \\ L_{n_{FE}} & 0 & 0 \\ 0 & L_1 & 0 \\ \vdots & \vdots & \vdots \\ 0 & L_{n_{FE}} & 0 \\ 0 & 0 & L_1 \\ \vdots & \vdots & \vdots \\ 0 & 0 & L_{n_{FE}} \end{bmatrix} \quad \text{and} \quad \mathbf{q} = \begin{bmatrix} q_1^1 \\ \vdots \\ q_{n_{FE}}^1 \\ q_1^2 \\ \vdots \\ q_{n_{FE}}^2 \\ q_1^3 \\ \vdots \\ q_{n_{FE}}^3 \end{bmatrix}, \tag{5}$$

In addition, note that $\mathbf{q}_I$ in (4) is the subset of $\mathbf{q}$ gathering the three components $\{q_I^1, q_I^2, q_I^3\}$ of the field $\mathbf{S}(\mathbf{X})$ associated to shape function L_I. Problem (2) is a non-linear least-square problem. Its resolution is based on a fixed point algorithm which consists in alternatively minimizing the graylevel functional j with respect to $\mathbf{p}$ (calibration) and to $\mathbf{q}$ (shape measurement). Herein, it may be mentioned that the alternating iterations are run until the stagnation of $(\mathbf{p}, \mathbf{q})$ is reached, whereas in the literature, only one iteration of the alternating minimization is usually performed. As will be seen in section 4, several iterations between the two minimization problems where necessary to properly measure a real shape far from the initial CAD.

Minimization with respect to camera parameters. The shape correction field $\mathbf{S}(\mathbf{X})$ being fixed, the set of parameters $\mathbf{p}$ is the solution of the calibration problem:

$$\mathbf{p}^\star = \underset{\mathbf{p}\in\mathbb{R}^{12}}{\arg\min}\ j(\mathbf{S}(\mathbf{X}),\mathbf{p}) \tag{6}$$

Such a non-linear least-square problem is solved using Gauss-Newton[48] iterations until the stagnation of $\mathbf{p}$, see[13] for details.

Minimization with respect to shape correction field. The extrinsic camera parameters $\mathbf{p}$ being fixed, the DOF vector $\mathbf{q}$ is the solution of the shape measurement problem:

$$\mathbf{q}^\star = \underset{\mathbf{q}\in\mathbb{R}^{3n_{FE}}}{\arg\min}\ j(\mathbf{L}^T(\mathbf{X})\ \mathbf{q},\mathbf{p}) \tag{7}$$

This non-linear least-square problem is also solved using a Gauss-Newton algorithm. At iteration k, the solution is sought as $\mathbf{q}^k = \mathbf{q}^{k-1} + \mathbf{d}_q^k$, where the descent direction $\mathbf{d}_q^k$ is the solution of the following linear system[13]:

$$\mathbf{H}_{FE}^k\mathbf{d}_q^k = \mathbf{b}_{FE}^k \qquad \text{with} \qquad \begin{cases} \mathbf{H}_{FE}^k = \displaystyle\int_{\Omega_s} \mathbf{L}\ (\mathbf{J}_0^{kT}\nabla\mathcal{I}_0^k - \mathbf{J}_1^{kT}\nabla\mathcal{I}_1^k)\ (\mathbf{J}_0^{kT}\nabla\mathcal{I}_0^k - \mathbf{J}_1^{kT}\nabla\mathcal{I}_1^k)^T\mathbf{L}^T\ \mathrm{d}\mathbf{X} \\ \mathbf{b}_{FE}^k = -\displaystyle\int_{\Omega_s} \mathbf{L}\ (\mathbf{J}_0^{kT}\nabla\mathcal{I}_0^k - \mathbf{J}_1^{kT}\nabla\mathcal{I}_1^k)\ r(\mathbf{L}^T\ \mathbf{q}^{k-1},\mathbf{p})\ \mathrm{d}\mathbf{X} \end{cases}, \tag{8}$$

$\nabla\mathcal{I}_c^k = \nabla\mathcal{I}_c(\mathbf{P}_c(\mathbf{X}+\mathbf{L}^T\mathbf{q}^{k-1}))$ with $\nabla\mathcal{I}_c$ defining the gradient of the graylevel image $\mathcal{I}_c$ and $\mathbf{J}_c^k = \mathbf{J}_c(\mathbf{X}+\mathbf{L}^T\mathbf{q}^{k-1})$ with $\mathbf{J}_c$ being the Jacobian of Projector $\mathbf{P}_c$ with respect to $\mathbf{X}$, *i.e.* such that $\mathbf{J}_{\mathbf{c}ij} = \partial\mathbf{P}_{\mathbf{c}i}/\partial X_j$. The so-called DIC operator $\mathbf{H}_{FE}^k$ is actually an approximation of the Hessian of j (using first-order derivatives only) and $-\mathbf{b}_{FE}^k$ corresponds to its gradient with respect to $\mathbf{q}$. To evaluate the integrals numerically, and since the quantities being integrated are not regular, a classical quadrature technique based on Riemann sums is used with approximately one integration point per pixel, see[49,13]. The Gauss-Newton loop is run until the stagnation of $\mathbf{q}$ is reached.

Remark 1. Up to now, the shape correction field was defined as homogeneous to a displacement field, with one component along each three dimension of space. But since a shape correction field tangent to the surface does not actually modify the geometry, Problem (8) is solved in projection onto the normal of the nominal surface. The shape correction field becomes a scalar field. The operator and right-hand side become $\mathbf{Z}^T\mathbf{H}_{FE}^k\mathbf{Z}$ and $\mathbf{Z}^T\mathbf{b}_{FE}^k$ respectively, with $\mathbf{Z}$ being a $3n_{FE}\times n_{FE}$ operator representing the normal.

Remark 2. During an experiment, change in illumination may occur, which may change locally the gray level values of images. In DIC which is based on a comparison of gray level values, such modulations are taken into account by an affine correction in gray levels[12]:

$$\widetilde{r}(\mathbf{S},\mathbf{p}) = \alpha\ r(\mathbf{S},\mathbf{p}) + \beta, \tag{9}$$

where α and β are adjusted to account for contrast and brightness modulations respectively. These values, usually taken constant in DIC, have to be considered as additional unknowns of the DIC problem. Shape and calibration rely on a measure of the discrepancy between gray levels of images taken by different cameras from different view angles. The issue of brightness and contrast modulation is much more acute. Choosing α and β as constants may be insufficient. In[12], α and β are sought as low order polynomials, but specular reflections may not be well described by low frequency corrections. In this paper, inspired from subset DIC methods, an elementary brightness and contrast adjustment is performed, considering α and β as piecewise constants. Images $\mathcal{I}_0$ and $\mathcal{I}_1$ are modified at each iteration such that their average is zero and their standard deviation is one, on each finite element.

Remark 3. As any Newton type algorithm, the question of the initial guess of $\mathbf{p}$ and $\mathbf{q}$ is crucial. On the one hand, as stated above, the theoretical shape is supposed to be a good approximation of the actual shape in experimental mechanics, therefore $\mathbf{q}=\mathbf{0}$ is a good initialization. On the other hand, the extrinsic parameters are not known. It is usually initialized by picking manually some (at least 3) points on the mesh and on each image. However, even under these conditions, and particularly when the discrepancy between theoretical and real shape is significant, a pyramidal multi-scale initialization technique may be relevant to improve convergence. In FE-SDIC, the idea consists in filtering images and regularizing the shape simultaneously. Instead of filtering images, pixel aggregation (to generate low-definition images) is probably the best idea because of computational speedup. More precisely, starting with coarse images and a high level of regularization, the process consists in decreasingly filtering the images while reducing the regularization level at each considered scale to reach the fine images. A classic way of regularizing is to

resort to Tikhonov regularization technique, *i.e.* to complement system (8) as follows:

$$(\mathbf{H}_{FE}^{k} + \lambda\ \mathbf{A})\ \mathbf{d}_{q}^{k} = \mathbf{b}_{FE}^{k} - \lambda\ \mathbf{A}\ \mathbf{q}^{k-1}, \tag{10}$$

where $\mathbf{A}$ is a linear operator such that $\mathbf{A}\ \mathbf{q}$ expresses the gradient of $\mathbf{S}(\mathbf{X})$ and λ is a penalization parameter whose value can be interpreted as the filter cutoff frequency (see, *e.g.*,[19,13] for more details). The larger λ, the higher the regularization level.

3 | GEOMETRIC REGULARIZATION BASED ON BÉZIER EXTRACTION

We now propose to geometrically regularize the FE mesh-based shape measurement problem (7) by projecting it onto more regular spline-based subspaces. We notice that spline functions have already been successfully used in DIC given their high degree of regularity (see, *e.g.*,[50,51,52,53,54]). In the context of shape measurement, their interest is expected to be even more important since these functions are particularly adapted to optimize free-form surfaces[36,37].

3.1 | Splines: basics and shape modification

The spline technology which has become a standard over the years for geometric modelling in CAD and computer graphics relies on the use of non-uniform rational B-spline (NURBS) functions[25,26,27]. Only the fundamentals are given in the following. For further details, the interested reader is referred to the references cited therein. The NURBS functions lend themselves to an exact representation of many shapes used in engineering, such as conical sections (circle, ellipse, etc). NURBS are a generalization of B-splines: they can be viewed as rational projections of B-splines. Therefore, they possess many of the properties of B-splines, the most interesting one being their increased smoothness, thus implying few degrees of freedom.

A general expression for a NURBS geometry with parameter $\boldsymbol{\xi} \in \mathbb{R}^d$ (d being the dimension of the space) is written as:

$$\boldsymbol{S}(\boldsymbol{\xi}) = \sum_{I=1}^{n_{IG}} R_I(\boldsymbol{\xi})\mathbf{x}_I = \mathbf{R}^T(\boldsymbol{\xi})\mathbf{x}, \tag{11}$$

where $\mathbf{R}$ and $\mathbf{x}$ denote the matrix of the n_{IG} NURBS basis functions and the vector collecting the location of the associated control points, respectively. Note that the same convention as in (4) is used here for the notation. The multivariate NURBS basis functions are obtained from the multivariate B-spline functions N_I as follows:

$$R_I(\boldsymbol{\xi}) = \frac{w_I N_I(\boldsymbol{\xi})}{W(\boldsymbol{\xi})} \quad \text{with} \quad W(\boldsymbol{\xi}) = \sum_{k=1}^{n_{IG}} w_k N_k(\boldsymbol{\xi}), \tag{12}$$

and where w_I denotes the weight of the I^{th} control point. Given Eq. (12) (and verifying that the B-spline functions satisfy the partition of unity), it may be noticed that if all weights are equal, the NURBS entity turns out to be a B-spline entity. Then, all one needs to do in order to define the multivariate B-spline function N_I at control point $\mathbf{x}_I$ is to perform the tensor product of the univariate B-spline functions associated with this point in the different spatial directions. Finally, the n_{IG_1} 1D B-spline basis functions are piecewise polynomials defined by their polynomial degree p and a set of non-decreasing parametric coordinates $\xi_i \in \mathbb{R}$ collected into a knot-vector $\Xi = \left\{\xi_1, \xi_2, .., \xi_{n_{IG_1}+p+1}\right\}$. From knot-vector Ξ, the B-spline basis functions are constructed recursively using the Cox-de Boor recursion formula (see Cohen *et al.*[25]). The coordinates ξ_i, referred to as knots, divide the parametric space into elements, and the interval $\left[\xi_1, \xi_{n_{IG_1}+p+1}\right]$ constitutes the patch. Unlike standard FE where each element has its own parametrization, the parametric space of B-spline functions is localized onto the patch, that may be thought of as a macro-element. Several patches can be assembled (similar procedures as for FE assembly) to model complex geometries. As illustrations, Figures 2(a) and 3(a) show two quadratic B-spline curves. These ones result from a linear combination of the univariate B-spline functions depicted at the bottom of Fig. 3(a) using, as coefficients, the control points marked with black circles on each figure. Degree $p = 2$ and knot-vector $\Xi = \{0, 0, 0, 0.5, 1, 1, 1\}$ are considered for the construction of the B-spline functions.

An interesting feature of splines is their high degree of regularity. If m is the multiplicity of a given knot, the functions are C^{p-m} continuous at that location, which is in contrast with standard FE where only a C^0 regularity is encountered on the element boundaries. This property is very appealing from the design point of view since it allows to define smooth free-form shapes using few degrees of freedom. Returning to Figs 2(a) and 3(a), it means that the regularity of the curve between the two elements

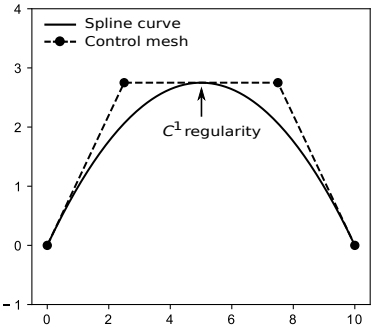

(a) Initial B-spline model (the control mesh is the linear interpolation of the control points).

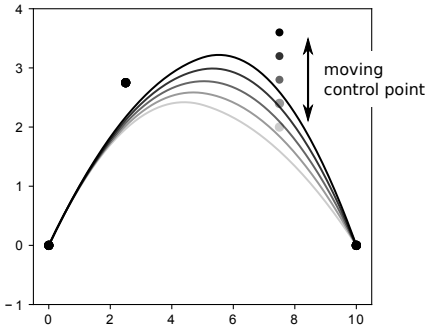

(b) Modification of the shape by moving vertically the third control point.

FIGURE 2 Spline generation and shape modification: example of a two-element quadratic C^1 B-spline curve.

is C^1. To modify the shape of the spline entities, one may thus simply need to move the control points, which results in a natural smooth modification of the geometry (see Fig 2(b) for illustration).

Furthermore, spline functions present refinement procedures which allow to enhance the design space (used for updating the shape) without changing the geometry. In particular, one may refine the spline mesh by inserting knots (knot-insertion technique) while maintaining the initial smooth shape (see Fig 3(b) for illustration). As a result, starting with a coarse spline model, the refinement of the design space can be chosen in accordance with the desired complexity of the final shape. Even more importantly, the modification of the shape can be performed using a multilevel strategy as in IG shape optimization[34,36]: one may begin with a coarse design model to fit the major tendencies of the surface and then refine the spline model to get the sharper variations. Eventually, note that matrix representations of the spline refinement procedures are possible; that is, denoting by $\mathbf{R}^c$ and $\mathbf{R}^f$ the matrices collecting, respectively, the n^c_{IG} coarse and n^f_{IG} fine spline functions, we can build the refinement operator $\mathbf{C}^{c,f}_r$ such that:

$$\mathbf{R}^c = \mathbf{C}^{c,f}_r \mathbf{R}^f \quad (n^c_{IG} \leq n^f_{IG}). \tag{13}$$

Such a relation offers a simple way to build the refined spline mesh from the coarse one. Denoting by $\mathbf{x}^c$ and $\mathbf{x}^f$ the location of the control points associated to the coarse and fine description, respectively, and asserting that the geometry (see Eq. (11)) is not modified through the refinement, we can write the following equality:

$$\left(\mathbf{R}^c(\boldsymbol{\xi})\right)^T \mathbf{x}^c = \left(\mathbf{R}^f(\boldsymbol{\xi})\right)^T \left(\mathbf{C}^{c,f}_r\right)^T \mathbf{x}^c, \quad \forall \boldsymbol{\xi} \ ; \tag{14}$$

which simply leads to:

$$\mathbf{x}^f = \left(\mathbf{C}^{c,f}_r\right)^T \mathbf{x}^c. \tag{15}$$

For more details on refinement strategies of splines and their matrix representations, reference is made to[26,39,55].

Remark 4. NURBS also offer the opportunity to apply shape variation by modifying the control point weights. Nevertheless, unless a very coarse NURBS model is considered[56,35], it appears from the IG shape optimization community that it is generally sufficient for free-form surfaces to only use the control point coordinates (see, *e.g.*, Kiendl *et al.* [36]). We perform similarly in this work.

Remark 5. In a general context, additional attention may be required when updating the shape for a rather fine spline geometric model. Indeed, if the control points are allowed to independently move in every spatial direction, fold-overs may appear. However, as noted in remark 1, only the normal component of the displacement is considered for the update of the geometry in this study, which naturally circumvents the problem.

3.2 | IG-FE bridge

Recalling that the desired input and output in our methodology is the fine (analysis-suitable) FE mesh, it is now required to establish a link between this FE mesh and the different (multilevel) spline-based descriptions introduced in previous section.

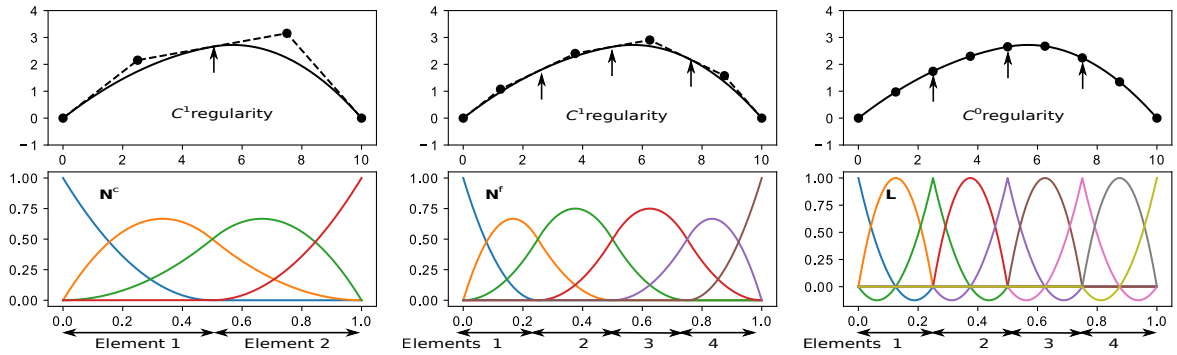

(a) Coarse B-spline model ($p = 2$, 2 elements, 4 control points, C^1 regularity at $\xi = 0.5$).

(b) Refined B-spline model (insertion of knots $\xi = 0.25$ and 0.75 so that: $p = 2$, 4 elements, 6 control points, C^1 regularity at $\xi = 0.25$, 0.5 and 0.75).

(c) Finite element model ($p = 2$, 4 standard $C^0 - C^0$ elements, 9 nodes)

FIGURE 3 Going from a coarse spline representation to a fine (analysis-suitable) FE mesh without modifying the initial geometry.

3.2.1 | Principle

The ultimate objective is to be able to build, in an explicit and non-invasive manner, the different Hessian and gradient operators, associated to the different spline approximation subspaces, from their fine FE counterparts computed using our FE-SDIC code (see Eqs. (8)). Since it is already possible to communicate between the different spline models (see Eqs. (13) and (15)), the goal here is to relate a fine FE and a fine spline discretization (*i.e.*, with same number of elements and same polynomial degree). In order to do so, we make use of previous work[41] in which a global algebraic bridge between IGA and FEA is constructed by resorting to Bézier-based operators[42,43]. More precisely, an operator that maps a C^0 FE basis onto a smooth spline basis can be formulated. Details regarding the construction of this operator are given in forthcoming sections 3.2.2 and 3.2.3.

Considering that we have such an operator in hand and denoting it by $\mathbf{C}_{FE}$, we can write:

$$\mathbf{R}^f = \mathbf{C}_{FE}\mathbf{L}, \tag{16}$$

($\mathbf{L}$ being the standard nodal Lagrange basis functions of Eq. (4)). As a result, following a similar procedure as in Eq. (14), we can build a FE mesh that fits with the spline geometric model by taking the location of the FE nodes $\mathbf{x}^{FE}$ as follows:

$$\mathbf{x}^{FE} = \mathbf{C}_{FE}^T\mathbf{x}^f. \tag{17}$$

As an example, this treatment has been performed to obtain the FE model of Fig. 3(c) starting with the spline model of Fig. 3(b). From the resulting FE mesh, we then have the opportunity to recover the refined spline Hessian and gradient operators without implementing IGA but simply by projecting the related FE operators onto the reduced, spline basis. Indeed, from Eq. (8), we can compute the associated spline operator $\mathbf{H}_{IG}^f$ such that (superscript k omitted):

$$\begin{aligned}\mathbf{H}_{IG}^f &= \int_{\Omega_s} \mathbf{R}^f(\mathbf{J}_0{}^T\nabla\mathcal{I}_0 - \mathbf{J}_1{}^T\nabla\mathcal{I}_1)\,(\mathbf{J}_0{}^T\nabla\mathcal{I}_0 - \mathbf{J}_1{}^T\nabla\mathcal{I}_1)^T\mathbf{R}^{fT}\,\mathrm{d}\mathbf{X}\\ &= \int_{\Omega_s} \mathbf{C}_{FE}\mathbf{L}\,(\mathbf{J}_0{}^T\nabla\mathcal{I}_0 - \mathbf{J}_1{}^T\nabla\mathcal{I}_1)\,(\mathbf{J}_0{}^T\nabla\mathcal{I}_0 - \mathbf{J}_1{}^T\nabla\mathcal{I}_1)^T\mathbf{L}^T\mathbf{C}_{FE}^T\,\mathrm{d}\mathbf{X}\\ &= \mathbf{C}_{FE}\,\mathbf{H}_{FE}\,\mathbf{C}_{FE}^T.\end{aligned} \tag{18}$$

As well, the spline gradient operator $\mathbf{b}_{IG}^f$ can be obtained from its FE counterpart $\mathbf{b}_{FE}$ (see Eq. (8)) as follows:

$$\mathbf{b}_{IG}^f = \mathbf{C}_{FE}\,\mathbf{b}_{FE}. \tag{19}$$

Furthermore, the same procedure can be applied to recover the coarse spline operators from the fine FE ones:

$$\begin{cases}\mathbf{H}_{IG}^c = \mathbf{C}_r^{c,f}\,\mathbf{H}_{IG}^f\,\left(\mathbf{C}_r^{c,f}\right)^T = \mathbf{C}_r^{c,f}\,\mathbf{C}_{FE}\,\mathbf{H}_{FE}\,\mathbf{C}_{FE}^T\,\left(\mathbf{C}_r^{c,f}\right)^T\\ \mathbf{b}_{IG}^c = \mathbf{C}_r^{c,f}\,\mathbf{b}_{IG}^f = \mathbf{C}_r^{c,f}\,\mathbf{C}_{FE}\,\mathbf{b}_{FE}\end{cases}. \tag{20}$$

Consequently, the IG regularized shape measurement systems of form $\mathbf{H}^c_{IG}\mathbf{d}_{q^c} = \mathbf{b}^c_{IG}$ and $\mathbf{H}^f_{IG}\mathbf{d}_{q^f} = \mathbf{b}^f_{IG}$ can be solved instead of the ill-posed fine FE shape measurement systems (8). Finally, note that the resulting IG DOF vectors, denoted by $\mathbf{q}^c$ or $\mathbf{q}^f$, can be back-converted in terms of nodal FE shape update $\mathbf{q}$:

$$\mathbf{q} = \mathbf{C}^T_{FE}\left(\mathbf{C}^{c,f}_r\right)^T\mathbf{q}^c \quad \text{or} \quad \mathbf{q} = \mathbf{C}^T_{FE}\mathbf{q}^f, \tag{21}$$

so that a unique basis is used for the representation of the surface at each multilevel step. An overview of the different transformations is given in Figure 4.

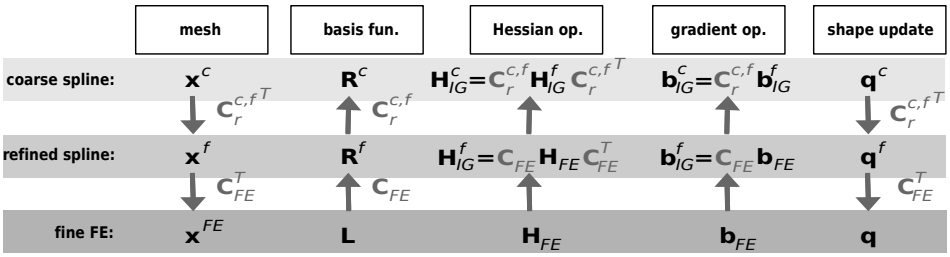

FIGURE 4 Overview of the different transformations enabling to communicate between the fine (analysis-suitable) FE mesh and the different (multilevel) spline-based discretizations.

3.2.2 | Construction: case of B-splines

In case of a B-spline geometric model, constructing $\mathbf{C}_{FE}$ appears quite straightforward since both spline and FE discretizations rely on polynomials. Indeed, since the space generated by the B-Spline functions (smooth polynomials) is included into the one generated by the Lagrange functions (C^0 polynomials), the process consists in extracting the smooth part of C^0 functions.

In order to form a multivariate C^0 mesh from a multivariate smooth B-spline mesh, the starting point consists in repeating all the inside knots of the knot-vectors until they reach a p multiplicity. A specific knot-insertion process is thus performed which enables to get the famous Bézier extraction operator whose interest to relate IGA and FEA has been intensely demonstrated (see[42,57,58,59,60] to name a few). More precisely, the Bézier extraction operator maps a Bernstein basis onto a B-Spline basis. Bernstein and Lagrange polynomials generates the same approximation subspace. Therefore, the second step consists in moving from the Lagrange basis to the Bernstein basis which can be easily performed by evaluating the Bernstein functions at the nodal points associated to the Lagrange basis. The succession of these two steps leads to the construction of the Lagrange extraction operator[43] that we denote $\mathbf{D}_{LAG}$ in the following. Consequently, we simply have $\mathbf{C}_{FE} = \mathbf{D}_{LAG}$ in case of B-splines. For more details regarding these transformations, the interested reader is advised to consult[41,42,43].

Remark 6. Note that for better numerical efficiency, the Lagrange extraction operator can be directly computed from the B-spline and Lagrange basis. Indeed, it merely requires to evaluate the B-spline basis functions at the nodal points of the Lagrange basis.

Remark 7. The present work is restricted to quadratic functions since almost all standard FE codes do not go beyond second-order Lagrange finite elements (the famous 9-node quadrilateral element in 2D, or the 27-node cubic element in 3D). Nevertheless, we emphasize that the proposed methodology could be directly applied to higher-order spline-based discretization, provided that the corresponding higher-order FE are available in a FE-SDIC environment.

3.2.3 | Construction: case of NURBS

As opposed to previous works on the subject that are restricted to B-splines[40,18,19], we undertake to also consider NURBS here to exactly represent conic sections. The Lagrange extraction can be extended to the case of NURBS but, it cannot directly go from a Lagrange basis to a NURBS basis since the first one is based on polynomials while the other one relies on rational functions. The NURBS version of the Lagrange extraction actually consists in mapping a rational Lagrange basis onto a NURBS basis, as detailed in[43]. To truly start with Lagrange polynomials, the construction of an additional mapping going from polynomials to rational functions is required. Such a transformation cannot be exact since this is the space of the rational functions that includes the associated polynomials and not the other way around. A projection thus needs to be performed. In order to do so, we propose

to proceed as in[41]; that is, we start with the NURBS version of the Lagrange extraction and then perform the projection at the Lagrange level. This offers the opportunity to follow a pragmatic yet accurate strategy.

More precisely, using the B-spline version of the Lagrange extraction operator and returning to (12), we can write:

$$\mathbf{R}^f(\boldsymbol{\xi}) = \frac{\mathbf{W}^f \mathbf{D}_{LAG} \mathbf{L}(\boldsymbol{\xi})}{W^f(\boldsymbol{\xi})}, \tag{22}$$

where $\mathbf{W}^f$ is the diagonal matrix collecting the weights of the refined NURBS discretization and $W^f(\boldsymbol{\xi}) = \sum_{k=1}^{n_{IG}^f} w_k^f N_k^f(\boldsymbol{\xi})$ is the associated NURBS weight function. Omitting dependency on $\boldsymbol{\xi}$, the NURBS weight function can be rewritten using the Lagrange basis as:

$$\begin{aligned} W^f &= \sum_{k=1}^{n_{IG}^f} w_k^f N_k^f = (\mathbf{w}^f)^T \mathbf{N}^f = (\mathbf{w}^f)^T \mathbf{D}_{LAG} \mathbf{L} \\ &= (\mathbf{D}_{LAG}^T \mathbf{w}^f)^T \mathbf{L} = (\mathbf{w}^{LAG})^T \mathbf{L} = W^{LAG}, \end{aligned} \tag{23}$$

where the weights associated to the rational Lagrange control points are:

$$\mathbf{w}^{LAG} = \mathbf{D}_{LAG}^T \mathbf{w}^f. \tag{24}$$

The rational Lagrange functions are then defined as follows:

$$\mathbf{R}^{LAG} = \frac{\mathbf{W}^{LAG} \mathbf{L}}{W^{LAG}}, \tag{25}$$

where $\mathbf{W}^{LAG}$ is the diagonal matrix of the Lagrange weights. The link between NURBS functions and rational Lagrange functions is finally made using Eqs. (25) and (23) in Eq. (22). Consequently, a new extraction operator $\mathbf{D}_{LAG}^W$ is created as described below:

$$\mathbf{R}^f = \mathbf{W}^f \mathbf{D}_{LAG} (\mathbf{W}^{LAG})^{-1} \mathbf{R}^{LAG} = \mathbf{D}_{LAG}^W \mathbf{R}^{LAG}. \tag{26}$$

Then, going from $\mathbf{L}$ to $\mathbf{R}^{LAG}$ or, in other terms, from $\mathbf{x}^{LAG}$ (the location of the rational Lagrange control points) to $\mathbf{x}^{FE}$, can be achieved very simply. Indeed, noticing that the control points of the rational Lagrange discretization interpolates the geometry, it appears possible to consider that the position of the FE nodes $\mathbf{x}^{FE}$ is exactly the same as the position of the rational Lagrange control points $\mathbf{x}^{LAG}$. Following this strategy, we end up with:

$$\mathbf{x}^{FE} \approx \left(\mathbf{D}_{LAG}^W\right)^T \mathbf{x}^f \quad \text{and} \quad \mathbf{R}^f \approx \mathbf{D}_{LAG}^W \mathbf{L}, \quad \textit{i.e.} \quad \mathbf{C}_{FE} = \mathbf{D}_{LAG}^W. \tag{27}$$

The above approximations get more accurate with the refinement of the NURBS mesh, which is assumed to be the case here since it is related to the last-level NURBS model. As demonstrated in[41], this process provides sufficient accuracy with already rather coarse NURBS meshes for typical engineering geometries.

3.3 | Proposed methodology

We now have all the ingredients in hand to present the proposed methodology. The objective is to improve the mesh-based shape measurement occurring in FE-SDIC by using, in a non-invasive manner, a geometrically sound regularization. In order to do so, the main idea is to relate the multilevel spline parametrizations of the geometry (and of its update) with the multi-scale images used for the initialization of the shape measurement (see remark 3). The principle is illustrated in Fig. 5. The different approximation subspaces that describe the geometry are chosen in accordance with the resolution of the images so that the shape measurement problem is regularized at each scale (number of DOF versus number of pixels). The coarse scales enable to fit the major tendencies of the surface while the finer ones allow the representation of sharper variations. Moving from scale s to finer scale $s-1$, the spline design space is enhanced while keeping the same geometry, and the initial solution for the shape measurement problem of scale $s-1$ is taken as the final solution of scale s.

Remark 8. In practice, the method starts from a sufficiently coarse representation of the nominal geometry. So far, in experimental mechanics, specimen's shape is relatively smooth such that very compact spline representations with very few DOF are generally sufficient. In a situation where the initial CAD representation should be too fine to effectively regularize the problem, it would be possible to either reduce the number of scales or resort to additional Tikhonov-type regularization techniques. Note that even in such a case, although insufficient a certain amount of geometric regularization is expected. Indeed, the level of Tikhonov regularization should presumably be lower than the one which would be required with an analysis-suitable FE mesh.

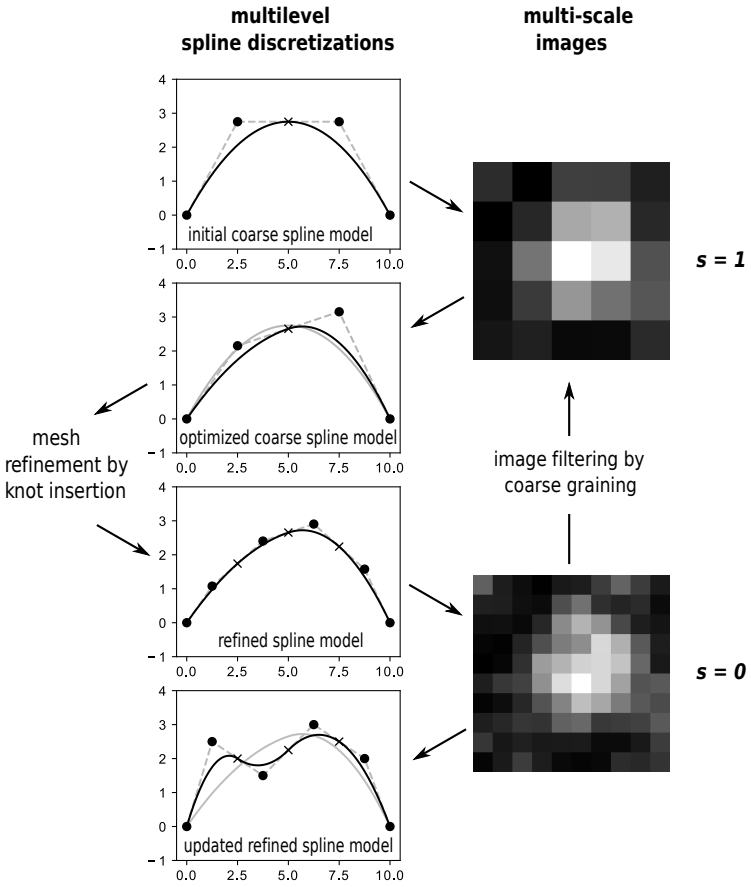

FIGURE 5 Principle of the geometric regularization: the multilevel spline optimization process is coupled with the multi-scale initialization of shape measurement.

More precisely, an overview of the proposed regularization scheme included in the calibration of the whole stereo rig is given in Fig. 6. For simplicity, we denote by $\mathbf{C}_s$ the extraction operator that maps the fine FE space onto the spline discretization of scale s, *i.e.* $\mathbf{C}_s$ is defined such that:

$$\mathbf{C}_0 = \mathbf{C}_{FE} \quad \text{and} \quad \mathbf{C}_s = \left(\prod_{i=0}^{s-1} \mathbf{C}_r^{(s-i),(s-i-1)} \right) \mathbf{C}_{FE}, \ \forall s \in \left\{ 1, .., n_s \right\}, \tag{28}$$

where n_s is the number of scales and $s = 0$ corresponds to the finest scale while $s = n_s$ refers to the coarsest scale. As can be observed, making use of the IG-FE bridge of previous section, the implementation is performed from standard FE-SDIC routines with minimal effort. Summarizing, we proceed as follows for the regularization. From the initial CAD representation of the theoretical surface, we build in the pre-processing step a fine analysis-suitable FE mesh and the different multilevel spline discretizations through their corresponding extraction operators $\mathbf{C}_s$. Then, entering into the shape measurement loop and beginning with the coarsest scale, we project, at each iteration of the Gauss-Newton solver, the FE hessian and gradient onto the first-level spline space and solve the associated regularized IG system. We thus end up with the IG shape update that can be converted in terms of nodal FE shape update so that the FE hessian and gradient can be updated for the next iteration. Going to the finest scale, we finally repeat the previous procedure with the different refined spline spaces to regularize at each scale. The final shape can be given either in terms of splines (thereby directly compatible with CAD environments) or in terms of finite elements (thus facilitating the communication with numerical simulations).

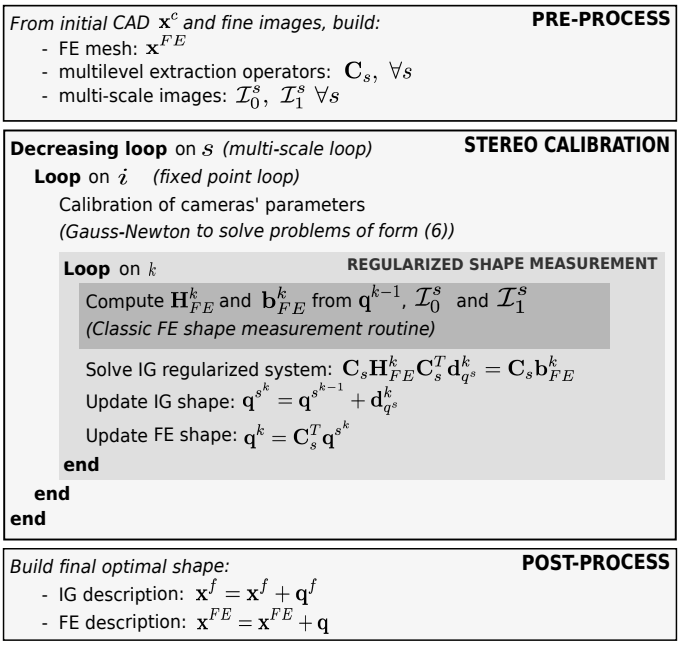

FIGURE 6 Overview of the proposed regularization scheme included in the calibration of a stereo rig.

4 | EXAMPLES

In this section, the proposed regularization technique for mesh-based shape measurement is applied to a real experiment. A steel open-hole tensile specimen of size $180 \times 50 \times 2$ mm and hole diameter 28 mm was considered. A dedicated speckle pattern was laser printed over a layer of uniform white paint. A pair of 5 Mpx CCD cameras and 50 mm lenses was used to capture the 8bit 2452x2052 digital images presented in Figure 1. The stereo-angle was set around 25° which represents a good compromise between in-plane and out-of-plane uncertainties[61]. The intrinsic parameters of the nonlinear camera models (first order radial distortions) were calibrated prior to the experiment using a series of digital images of a calibration target made of a grid of 12x9 dots with a step size of 3 mm. The obtained intrinsic parameters are considered fixed in the remainder of the study. More precisely, two configurations were considered for the study:

- In a chronological order, the specimen was first clamped in the lower jaw of an electro-mechanical tensile testing machine. The upper part of the specimen was left free. In this first configuration, a set of images was taken and is referred to as the *flat* configuration, as the observed surface of the specimen was almost plane. This configuration is used to analyse the robustness of the method to a reasonably complex shape.

- The specimen was then clamped in the upper jaw. Since the jaws are slightly misaligned, the hyper-static clamping generated a torsional moment and the specimen twisted. The misalignment was around 2 or 3° which should generate significant waviness. The corresponding set of images is referred to as the *twisted* configuration. With this case study, it is possible to analyze the method in a configuration where the difference between the theoretical (considered flat) and real (twisted) shapes is significantly greater than in standard mechanical experiments.

For a clear understanding of the results, we choose in the following to start with the twisted configuration and then turn to the flat configuration. The two pairs of digital images are analysed by (a) the proposed geometric, Bézier-based, regularized shape measurement method, (b) a standard FE-based shape measurement possibly considering Tikhonov regularization and (c) a more standard subset-based DIC method. It must be mentioned, at this stage, that the regions of interest of the FE-based and subset DIC are not equal. Indeed, the FE (or IG) meshes do conform to the edges of the specimen, whereas subset DIC was not able to perform shape measurement too close to the boundaries. This point should be kept in mind when comparing global and local DIC solutions.

4.1 | Pre-processing: construction of the geometric model and FE mesh

The nominal geometry of the sample consists in a plate with a circular hole. As a result, its exact representation in CAD requires the use of NURBS (rational B-splines). It is common to proceed as in Figure 7(a) for the building of the first NURBS model of such a geometry. Given that the four vertices of the plate imply a C^0 regularity of the geometry at those points, the coarsest NURBS model necessarily involves 4 C^0-C^0 elements. More precisely, denoting by ξ the parameter describing the circumferential direction, we needed to start with degree $p = 2$ in that direction with knot-vector $\Xi = \{0, 0, 0, 0.25, 0.25, 0.5, 0.5, 0.75, 0.75, 1, 1, 1\}$ (for more details on NURBS constructions, see, *e.g.*,[33]). Along the other direction, even if degree 1 would be sufficient, we also took degree 2 so as to be consistent with the final FE-mesh that is made of standard 9-node (*i.e.* bi-quadratic) elements. Starting with the NURBS model composed of 4 quadratic elements, we thus only performed knot-insertion (inserting one knot at a time) to get the different (multilevel) NURBS parametrizations (see Figs 7(b) and (c)). We finally further carried out knot-insertion and applied the IG-FE mapping of section 3.2 (see Eq. (17)) to obtain the analysis-suitable FE-mesh (see Figure 7(d)).

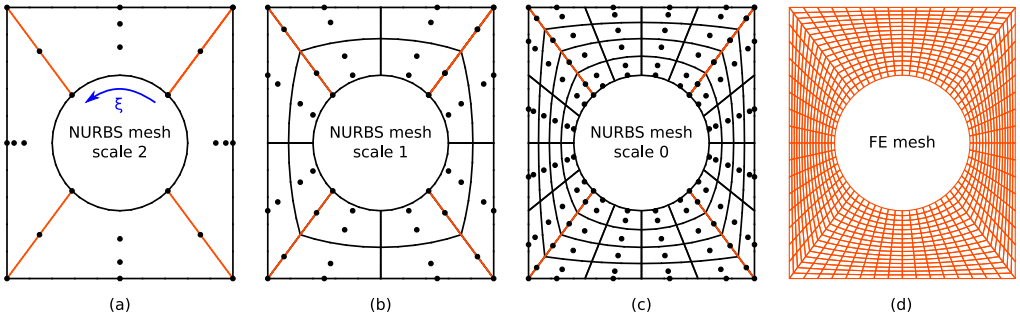

FIGURE 7 Initial CAD parametrization, mutli-level NURBS meshes and final fine FE mesh. The C^0 lines are orange. The final FE mesh is composed of 1000 elements.

Remark 9. Let us recall here that although a NURBS parametrization is used to represent exactly the in-plane geometry, the shape optimization with the proposed strategy only acts on the out-of-plane locations of the control points (see remark 4). As a result, the modification of the shape should not be interpreted as a NURBS modification but rather as some "spline" modification with fixed weights. We believe that the measurement uncertainties must certainly be greater than the difference between NURBS and B-Spline modifications. Now, given that the computational cost associated to $\mathbf{D}_{LAG}$ and $\mathbf{D}^W_{LAG}$ is similar (only two additional diagonal-matrix/matrix products for $\mathbf{D}^W_{LAG}$, see Eq. (26)) and that we simply have a practical NURBS parametrization of the nominal plate with a hole, we decided to use a NURBS instead of an approximate B-Spline parametrization for the nominal geometry here.

4.2 | Results : twisted configuration

Let us recall that, because of the misalignment of the jaws, in this clamped-clamped configuration, the specimen underwent a significant twist. Note that theses images were not analysed for displacement measurement using FE-SDIC with respect to the flat configuration images. They were used for shape measurement independently as if this configuration was the initial state of the specimen.

4.2.1 | Classic FE-based shape measurement without any regularization

A first classic FE shape measurement was performed using the FE mesh given in Figure 7(d) without any regularization. The obtained shape is represented in Figure 8. In order to compare the shape measurements obtained with the different considered techniques, we chose the color data to represent the distance to the best fitting plane (BFP) instead of directly plotting the shape correction field $\mathbf{S}(\mathbf{X})$ which would not be available using the subset approach. The shape is typical of a twist test. The waviness is around one millimeter, which, at the scale of this specimen, is large. In addition, the resulting shape is relatively noisy. Even tough the noise is one order of magnitude smaller than the artificially large shape correction field, it still seems large and unphysical.

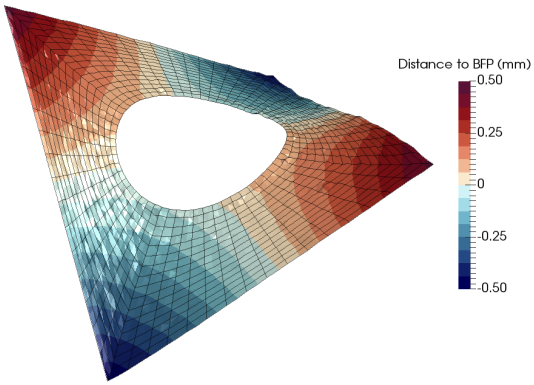

FIGURE 8 Twisted specimen: shape obtained with classic FE-SDIC without regularization (def. scale fact. x30).

4.2.2 | Use of standard Tikhonov regularization

In order to regularize this noise, a classic Tikhonov regularization technique was first considered. The shape obtained for three different regularization lengths is given in Figure 9. As expected, using Tikhonov regularization, the shape measurements

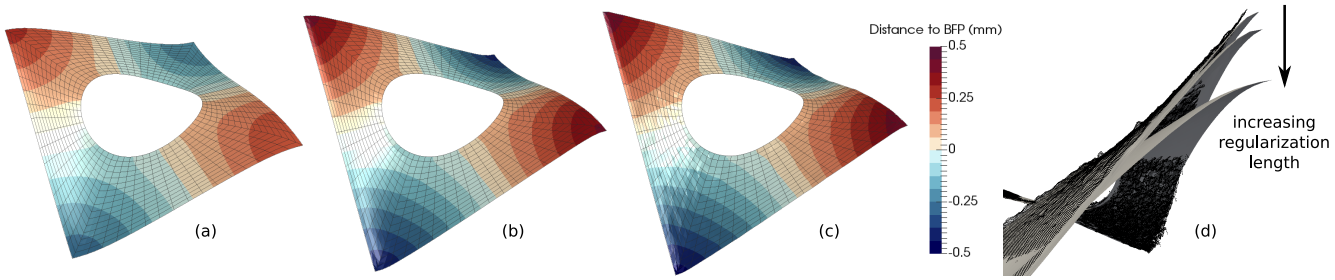

FIGURE 9 Twisted specimen: shape obtained using a classic FE-SDIC with Tikhonov regularization for different values of the regularization length: decreasing values of the regularization length from (a) to (c) respectively (def. scale fact. x30).

appeared clearly smoother, especially for large values of the regularization length (see Figs. 9(a) and (b)). It can be seen that such high levels of regularization may also affect the shape. Indeed, on Figure 9(d), the influence of the regularization length on the shape is depicted, with the subset approach as the reference. Using a too large regularization length reduces the displacement magnitudes and underestimates the shape waviness. Asymptotically, using very large values of regularization would lead to an almost constant correction field, which would correspond to a rigid body translation of the observed surface with respect to the theoretical CAD.

Conversely, for lower values of the regularization length, the solution looks more like the shape obtained without regularization. For instance Shape 9(c) is less noisy than the one illustrated in Figure 8, but high frequency noise is still present, which means that the regularization was still not sufficient. Even in this case, where the regularization level was insufficient to get completely rid of noise, it can be observed on Figure 9(d) that the correction field at the top corner was already underestimated because of the differential nature of the chosen regularization term. As shown in this example, choosing the correct regularization length value may become a tricky trade-off. In other words, a satisfying value of the regularization length may not exist, as it seems to be the case here.

4.2.3 | Use of the proposed geometric regularization

Next, the proposed geometric regularization scheme was considered with the same image set. The multi-scale initialization technique described in section 3.3 was applied with three scales using the three NURBS meshes of Figure 7. The corresponding shapes obtained at each scale are given in Figure 10.

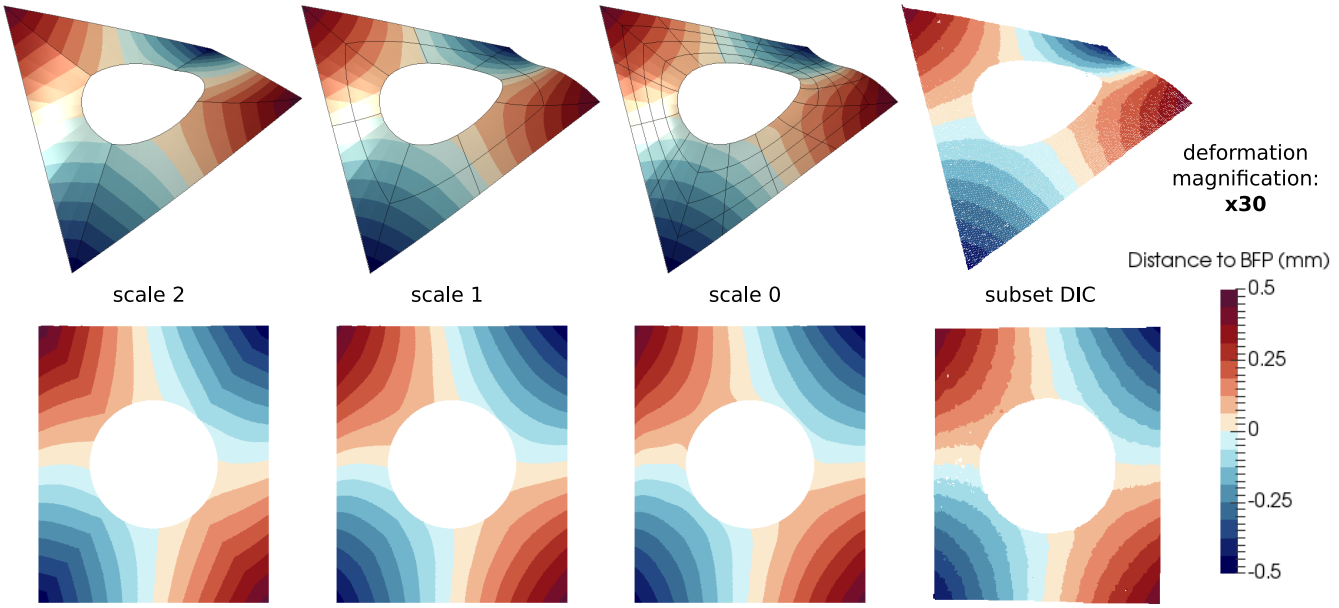

FIGURE 10 Twisted specimen with the proposed geometric regularization (def. scale fact. x30).

First, it can be observed that the shapes obtained at the three scales are very smooth. Indeed, the very low-dimensional spline approximation subspace acts as a very strong regularization technique. Each of the three shapes are very similar to each other and also in good agreement with the shape provided by the subset DIC method. In addition, the reduction in the correction field's magnitude observed when using the Tikhonov regularization did not occur here. Even at the highest scale, where the spline representation is particularly coarse, a very good approximation of the shape was already obtained. This property of the geometric regularization is particularly interesting for the highest scales of the multi-scale approach, since they are associated to high regularization levels.

Figure 11(left) presents the evolution of the standard deviation of the graylevel residual field in percent of the reference image dynamics (later denoted *relative residual*) as a function of the iteration number. It compares the convergence of the problem

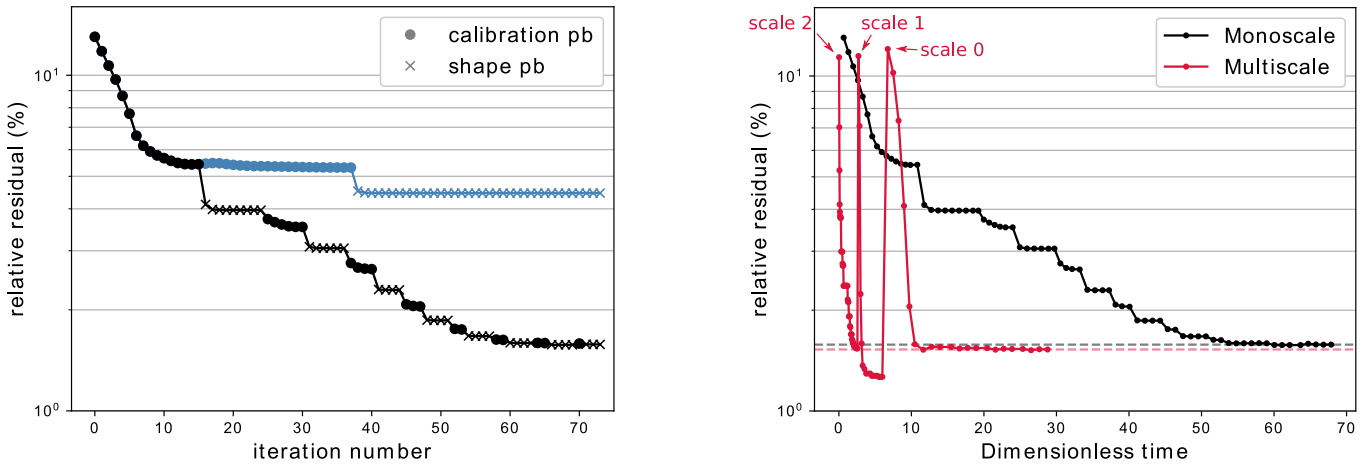

FIGURE 11 Convergence of the algorithm on the twisted use case: (left) convergence (vs iterations) of the relative residual with (black) and without (blue) the fixed point iterations and (right) convergence speed (vs dimensionless time) for the monoscale and multi-scale approaches.

with and without iterating between calibration of extrinsic parameters (• symbols) and shape correction problems (× symbols).

It can be seen that, at least on this case, converging the fixed point algorithm (by alternating between calibration and shape problems) is mandatory to converge towards an accurate solution. It is the case here because the actual shape is significantly different from the initial CAD. On the (right) side of the same figure, the relative residual is plotted as a function of the CPU time normalized by the CPU time taken by one iteration at scale 0, for the monoscale (only scale 0) and multi-scale approaches. It can be seen that, although the number of iterations may increase, the computational time is clearly reduced (divided by 2 in this case), since the higher scales are associated to low definition images whose interpolation is far cheaper. Note also, that when using the multi-scale approach, the value of the relative residual was lower than that of the monoscale alternative. Lower relative residual emerges from the fact that the multiscale initialisation, in addition to convergence acceleration, was designed to avoid local minima. In this example, the solutions seem to be similar, but the multi-scale approach, by avoiding local minima, may allow to reduce significantly the relative residual and therefore improve the measurement accuracy.

Remark 10. Note that the residual at scale $s > 0$ was estimated using the coarsened images and not with the full resolution (scale 0) images, for efficiency. This explains why the estimated residual at scale $s > 0$ is sometimes a little smaller than the one at scale 0 after convergence on Figure 11(right).

4.2.4 | A note regarding brightness and contrast correction

Another interesting point with this test case is the analysis of the graylevel residual field $r(\mathbf{S}(\mathbf{X}), \mathbf{p})$ at scale $s = 0$ before and after convergence, with and without elementary brightness and contrast correction. First, the initial graylevel map, obtained with the initial CAD (flat) shape and the initial set of extrinsic parameters, is depicted in Figure 12. Its value is about 70% of the

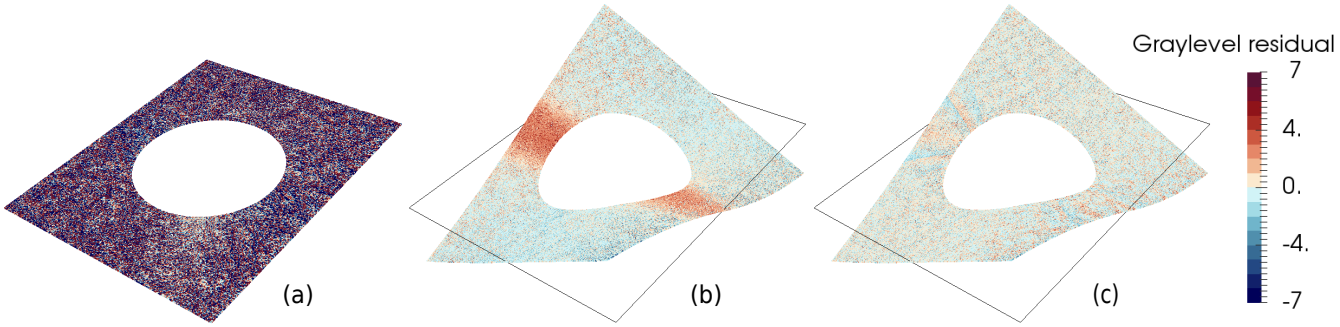

FIGURE 12 Graylevel residual $r(\mathbf{S}(\mathbf{X}), \mathbf{p})$ in percent of the dynamic of the images with (a) the initial CAD shape and after convergence (b) without and (c) with elementary brightness and contrast correction (def. scale fact. x30).

dynamic of the image which means that the graylevels do not correspond at all. After 8 iterations of the fixed point algorithm, the graylevel residual dropped to less than 10% of the images dynamic. It means that the graylevel conservation was correctly verified. It can be seen on Figure 12(b) that the residual map presents a band of higher value located around the hole when using a global brightness/contrast correction. This localized bad verification of the graylevel conservation was attributed to the presence of a specular reflection of the light which seems consistent with the twisting of the specimen. This phenomenon locally modifies the brightness and contrast (B/C). As shown here, global B/C correction methods can not take this into account. The proposed elementary B/C correction method (see remark 2) was applied and the resulting graylevel residual is depicted on Figure 12(c). It presents a homogeneous value around 2% of the dynamic in all the region of interest. This elementary correction technique is very simple but generic. It was shown that it can efficiently account for a complex local B/C variations which would be difficult using a global descriptor.

4.3 | Results : flat configuration

In this section, the so-called flat configuration where the specimen is clamped at the bottom end only is being analysed. Since here the specimen is nearly flat, the shape correction field is expected to be of lower magnitude, but less regular than the twist

of the previous section. Only the final shape measurements are plotted in this section to study the robustness of the geometric regularization method with respect to a more complex shape with lower signal to noise ratio. Figure 13 presents the shape measurement and distance to BFP when using (a) the FE-SDIC approach without regularization, (b) the local SDIC method and (c) the geometric regularization technique. First it can be noticed that all the shapes are in good agreement with each other. Note

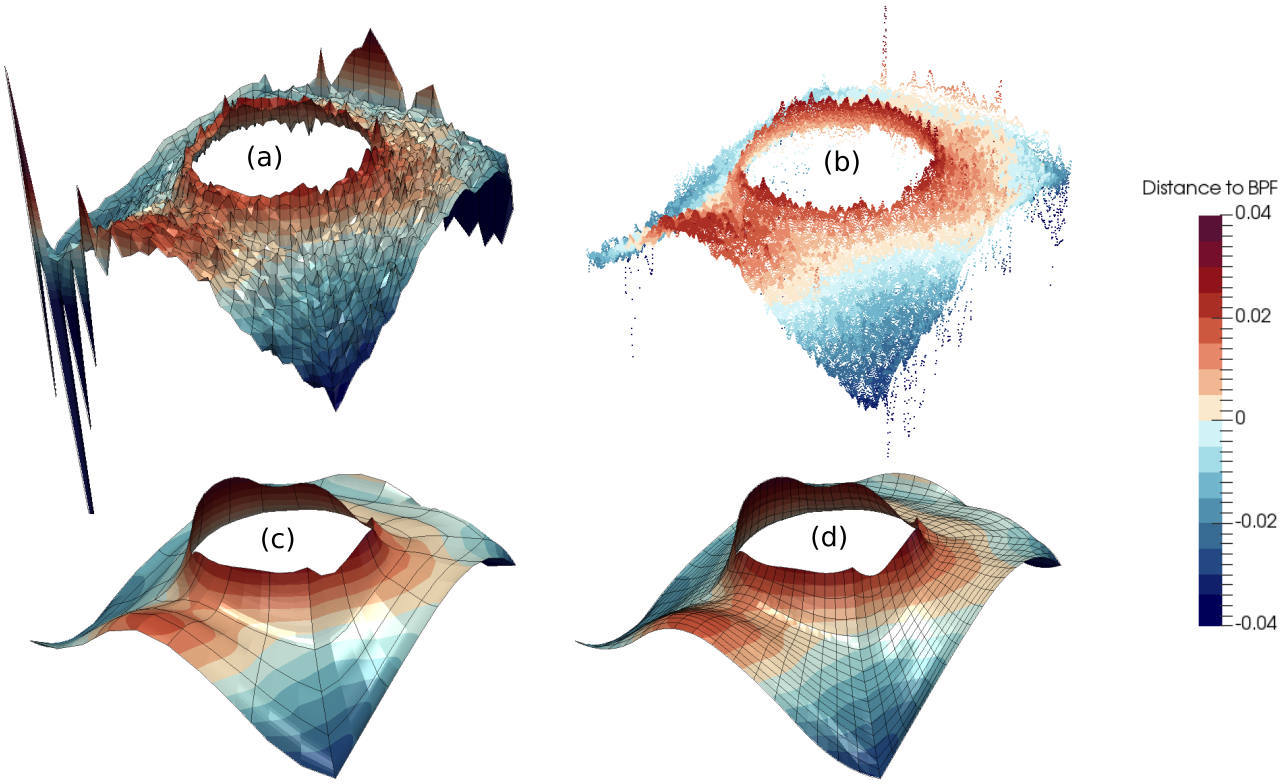

FIGURE 13 Flat specimen shapes with distance to best fitting plane (BFP) in mm: (a) measured by the FE-SDIC without regularization, (b) measured using the subset based SDIC and measured using the proposed geometric regularization: (c) Spline parametrization of the optimal shape and (d) corresponding measured finite element mesh (def. scale fact. x300).

that the waviness is one order of magnitude smaller than in the twist case. The FE and local SDIC measurements are clearly affected by noise. The geometric regularization technique efficiently manages to extract a regular shape from the images. From this measurement which provides the NURBS parametrization of the optimal shape, and using the IG-FE bridge of section 3.2, it is possible to build directly the FE mesh (see Figure 8(d)) which exactly corresponds to the same shape. Such an output may be convenient to be used for FE-SDIC displacement measurements in the context of validation/identification of FE models.

5 | CONCLUSION

In this paper, we developed a hybrid IG-FE strategy for the regularization of the mesh-based shape measurement occurring in FE-SDIC. From a regularization point of view, the proposed strategy draws inspiration from the techniques developed recently in the isogeometric shape optimization community, especially with the multilevel design concept[36,37,38]. By making use of the advanced spline refinement procedures and of adequate Bézier-based operators, the main idea here was to extract, from the initial FE subspace, smoother multilevel spline parametrizations of the geometry and to relate them with the multi-scale images used for the initialization of shape measurement. This treatment enabled to efficiently regularize, with a geometrical meaning, the problem at each scale. From a practical point of view, the proposed approach consists of nothing more than projecting the

ill-posed FE shape measurement problem onto more regular spline subspaces by using appropriate operators. But among the possible reduced bases which may regularize the FE shape problem, the one presented here yields the IG Hessian operator that has the great advantages to be geometrically sound and sparse. As a result, we ended up with a technique that draws up the best of IG and FE technologies. On the one hand, we benefit from the increased smoothness of spline functions for the description of the geometry and of its update. On the other hand, we can perform the resolution in a non-invasive manner from an existing FE-SDIC code and, we are able to describe the final shape using the same fine FE mesh as the one which could be used for displacement measurement and identification of mechanical models.

The performance of the developed methodology over existing strategies was demonstrated through the analysis of real images coming from different experiments. For each experiment, multilevel NURBS parametrizations of the geometry were built in accordance with the multi-scale images used for the initialization of the shape measurement. The method was implemented from existing FE-SDIC routines with minimal efforts. Our results clearly indicated the superiority of the proposed geometric regularization, especially as the real and the theoretical shapes are far from each other. We always managed to obtain a consistent smooth final shape within a limited number of iterations, while the standard Tikhonov regularization appeared to fail when rotations were expected. In addition, we outlined some other details of the mesh-based shape measurement process such as the importance of converging the (calibration/shape) fixed point. A new local brightness and contrast correction technique was also introduced herein.

Using recent progress in the field of Bézier extraction for local refinement[59,60], the considered IG-FE bridge[41] may be extended to start with a locally refined NURBS or B-Spline mesh. This would allow to derive an adaptive refinement strategy for S-DIC, similarly as what was performed in[54] for 2D-DIC. We finally notice that the proposed implementation procedure based on such IG-FE bridges for simply communicating between (possibly rational) spline spaces and a finer FE one may also be interesting in other contexts. For instance, such treatment could be applied to CAD-based shape optimization to naturally relate the (spline-based) design and (FE-based) analysis spaces[62].

References

1. Y. Sun, J. Pang, C. K. Wong, F. Su, Finite element formulation for a digital image correlation method, Applied Optics 44 (34) (2005) 7357–7363.

2. G. Besnard, F. Hild, S. Roux, "finite-element" displacement fields analysis from digital images: Application to Portevin-le Châtelier bands, Experimental Mechanics 46 (6) (2006) 789–803.

3. J. Réthoré, A fully integrated noise robust strategy for the identification of constitutive laws from digital images, International Journal for Numerical Methods in Engineering 84 (6) (2010) 631–660.

4. R. Fedele, L. Galantucci, A. Ciani, Global 2D digital image correlation for motion estimation in a finite element framework: a variational formulation and a regularized, pyramidal, multi-grid implementation, International Journal for Numerical Methods in Engineering 96 (12) (2013) 739–762.

5. A. Baldi, L. Francesconi, A. Medda, F. Bertolino, Comparing two damage models under shear stress, Experimental Mechanics 53 (7) (2013) 1105–1116.

6. J.-C. Passieux, F. Bugarin, C. David, J.-N. Périé, L. Robert, Multiscale displacement field measurement using digital image correlation: Application to the identification of elastic properties, Experimental Mechanics 55 (1) (2015) 121–137.

7. J. Van Beeck, J. Neggers, P. Schreurs, J. Hoefnagels, M. Geers, Quantification of three-dimensional surface deformation using global digital image correlation, Experimental Mechanics 54 (4) (2014) 557–570.

8. L. Wittevrongel, P. Lava, S. Lomov, D. Debruyne, A self adaptive global digital image correlation algorithm, Experimental Mechanics 55 (2) (2015) 361–378.

9. B. Blaysat, M. Grédiac, F. Sur, On the propagation of camera sensor noise to displacement maps obtained by DIC - an experimental study, Experimental Mechanics 56 (6) (2016) 919–944.

10. R. Bouclier, J.-C. Passieux, A domain coupling method for finite element digital image correlation with mechanical regularization: Application to multiscale measurements and parallel computing, International Journal for Numerical Methods in Engineering 111 (2) (2017), 123–143.

11. J. Réthoré, Muhibullah, T. Elguedj, M. Coret, P. Chaudet, A. Combescure, Robust identification of elasto-plastic constitutive law parameters from digital image using 3D kinematics, Int. J. Solids and Structures 50 (2013) 73–85.

12. J.-E. Dufour, F. Hild, S. Roux, Shape, displacement and mechanical properties from isogeometric multiview stereocorrelation, The Journal of Strain Analysis for Engineering Design 50 (7) (2015) 470–487.

13. J.-E. Pierré, J.-C. Passieux, J.-N. Périé, Finite element stereo digital image correlation: framework and mechanical regularization, Experimental Mechanics 53 (7) (2017) 443–456.

14. J. Serra, J.-E. Pierré, J.-C. Passieux, J.-N. Périé, C. Bouvet, B. Castanié, Validation and modeling of aeronautical composite structures subjected to combined loadings: the vertex project. Part 1: Experimental setup, FE-DIC instrumentation and procedures, Composite Structures 179 (2017) 224–244.

15. J.-C. Passieux, R. Bouclier, and J.-N. Périé, A space-time PGD-DIC algorithm: Application to 3d mode shapes measurements, Experimental Mechanics, 58(7) (2018) 1195–1206.

16. B. Lucas, T. Kanade, An iterative image registration technique with an application to stereo vision, in: Proceedings of Imaging Understanding Workshop, 1981, pp. 121–130.

17. D. Garcia, J.-J. Orteu, L. Penazzi, A combined temporal tracking and stereo-correlation technique for accurate measurement of 3D displacements: Application to sheet metal forming, Journal of Materials Processing Technology 125-126 (2002) 736–742.

18. J.-E. Dufour, B. Beaubier, F. Hild, S. Roux, CAD-based displacement measurements with Stereo-DIC, Experimental Mechanics 55 (9) (2015) 1657–1668.

19. J.-E. Dufour, S. Leclercq, J. Schneider, S. Roux, F. Hild, 3D surface measurements with isogeometric stereocorrelation âĂŤ application to complex shapes, Optics and Lasers in Engineering 87 (2016) 146 – 155.

20. J. Serra, J.-E. Pierré, J.-C. Passieux, J.-N. Périé, C. Bouvet, B. Castanié, C. Petiot, Validation and modeling of aeronautical composite structures subjected to combined loadings: the vertex project. Part 2: Load envelopes for the assessment of panels with large notches, Composite Structures 180 (2017) 550–567.

21. R. Haftka, R. Grandhi, Structural shape optimization – a survey, Computer Methods in Applied Mechanics and Engineering 57 (1) (1986) 91–106.

22. R. Haftka, Z. Gürdal, Elements of Structural Optimization, Third revised and expanded ed., Kluwer Academic Publishers, 1993.

23. M. Firl, R. WÃijchner, K.-U. Bletzinger, Regularization of shape optimization problems using FE-based parametrization, Structural and Multidisciplinary Optimization 47 (2013) 507–521.

24. K.-U. Bletzinger, A consistent frame for sensitivity filtering and the vertex assigned morphing of optimal shape, Structural and Multidisciplinary Optimization 49 (6) (2014) 873–895.

25. E. Cohen, T. Lyche, R. Riesenfeld, Discrete B-spline and subdivision techniques in computer aided geometric design and computer graphics, Computer Graphics and Image Processing 14 (1980) 87–111.

26. L. Piegl, W. Tiller, The NURBS book, 2Nd. Springer, New york, 1997.

27. G. Farin, Curves and surfaces for CAGD: a practical guide, Morgan Kaufmann Publishers Inc., San Francisco, 2002.

28. V. Braibant, C. Fleury, Shape optimal design using B-spline, Computer Methods in Applied Mechanics and Engineering 44 (1984) 247–267.

29. N. Olhoff, M. Bendsøe, J. Rasmussen, On CAD-integrated structural topology and design optimization, Computer Methods in Applied Mechanics and Engineering 89 (1991) 259–279.

30. M. Hasan Imam, Three-dimensional shape optimization, International Journal for Numerical Methods in Engineering 18 (1982) 661 – 673.

31. K.-U. Bletzinger, S. Kimmich, E. Ramm, Efficient modeling in shape optimal design, Computing Systems in Engineering 2 (1992) 483–495.

32. T. J. R. Hughes, J. A. Cottrell, Y. Bazilevs, Isogeometric analysis: CAD, finite elements, NURBS, exact geometry and mesh refinement, Computer Methods in Applied Mechanics and Engineering 194 (2005) 4135–4195.

33. J. A. Cottrell, T. J. R. Hughes, Y. Bazilevs, Isogeometric analysis: toward Integration of CAD and FEA, 1st edn. Wiley, 2009.

34. A. P. Nagy, M. M. Abdalla, Z. Gürdal, Isogeometric design of elastic arches for maximum fundamental frequency, Structural and Multidisciplinary Optimization 43 (1) (2011) 135–149.

35. A. P. Nagy, S. Ijsselmuiden, M. Abdalla, Isogeometric design of anisotropic shells: Optimal form and material distribution, Computer Methods in Applied Mechanics and Engineering 264 (2013) 145–162.

36. J. Kiendl, R. Schmidt, R. WÃijchner, K.-U. Bletzinger, Isogeometric shape optimization of shells using semi-analytical sensitivity analysis and sensitivity weighting, Computer Methods in Applied Mechanics and Engineering 274 (2014) 148–167.

37. T. Hirschler, R. Bouclier, A. Duval, T. Elguedj, J. Morlier, Isogeometric sizing and shape optimization of thin structures with a solid-shell approach, Structural and Multidisciplinary Optimization 59 (3) (2019) 767–785.

38. Y. Wang, Z. Wang, Z. Xia, L. H. Poh, Structural design optimization using isogeometric analysis: A comprehensive review, Computer Modeling in Engineering and Sciences 117 (2018) 455–507.

39. J. A. Cottrell, T. J. R. Hughes, A. Reali, Studies of refinement and continuity in isogeometric structural analysis, Computer Methods in Applied Mechanics and Engineering 196 (2007) 4160–4183.

40. B. Beaubier, J. E. Dufour, F. Hild, S. Roux, S. Lavernhe, K. Lavernhe-Taillard, CAD-based calibration and shape measurement with StereoDIC - principle and application on test and industrial parts, Experimental Mechanics 54 (3) (2014) 329–341.

41. M. Tirvaudey, R. Bouclier, J. C. Passieux, L. Chamoin, Non-invasive implementation of nonlinear Isogeometric Analysis in an industrial FE software, Engineering Computations, doi: 10.1108/EC-03-2019-0108.

42. M. Borden, M. A. Scott, J. A. Evans, T. J. R. Hughes, Isogeometric finite element data structures based on Bézier extraction of NURBS, International Journal for Numerical Methods in Engineering 87 (2011) 15 – 47.

43. D. Schillinger, P. K. Ruthala, L. H. Nguyen, Lagrange extraction and projection for NURBS basis functions: A direct link between isogeometric and standard nodal finite element formulations, International Journal for Numerical Methods in Engineering 108 (2016) 515–534.

44. M. A. Sutton, W. Zhao, S. R. McNeill, J. D. Helm, R. S. Piascik, W. T. Riddel, Local crack closure measurements: Development of a measurement system using computer vision and a far-field microscope, in: Advances in fatigue crack closure measurement and analysis: second volume, STP 1343 , R. C. McClung and J. C. Newman Jr., eds., 1999, pp. 145–156.

45. J.-M. Lavest, M. Viala, M. Dhome, Do we really need an accurate calibration pattern to achieve a reliable camera calibration?, in: H. Burkhardt, B. Neumann (Eds.), Computer Vision — ECCV'98, Springer Berlin Heidelberg, Berlin, Heidelberg, 1998, pp. 158–174.

46. D. Garcia, Mesure de formes et de champs de déplacements tridimensionnels par stéréo-corrélation d'images, Ph.D. thesis, Institut National Polytechnique de Toulouse (2001).

47. B. Horn, G. Schunck, Determining optical flow, Artificial Intelligence 17 (1981) 185–203.

48. J.-C. Passieux, R. Bouclier, Classic and Inverse Compositional Gauss-Newton in Global DIC, International Journal for Numerical Methods in Engineering, DOI: 10.1002/nme.6057.

49. J.-E. Pierré, J.-C. Passieux, J.-N. Périé, Unstructured Finite Element-based Digital Image Correlation with enhanced management of quadrature and lens distortions, Optics and Lasers in Engineering 77 (2016) 44–53.

50. P. Cheng, M. Sutton, H. Schreier, S. R. McNeill, Full-field speckle pattern image correlation with B-Spline deformation function, Experimental mechanics 42 (3) (2002) 344–352.

51. Z. Xie, G. E. Farin, Image registration using hierarchical b-splines, IEEE Transactions on Visualization and Computer Graphics 10 (1) (2004) 85–94.

52. T. Elguedj, J. Réthoré, A. Buteri, Isogeometric analysis for strain field measurements., Computer Methods in Applied Mechanics and Engineering 200 (1-4) (2010) 40–56.

53. J. Réthoré, T. Elguedj, P. Simon, M. Coret, On the use of NURBS functions for displacement derivatives measurement by digital image correlation, Experimental Mechanics 50 (2010) 1099–1116.

54. S. M. Kleinendorst, J. P. M. Hoefnagels, C. V. Verhoosel, A. P. Ruybalid, On the use of adaptive refinement in Isogeometric Digital Image Correlation, International Journal for Numerical Methods in Engineering 104 (10) (2015) 944–962.

55. B. G. Lee, Y. Park, Degree elevation of NURBS curves by weighted blossom, The Korean Journal of Computational & Applied Mathematics 9 (2002) 151–165.

56. X. Qian, Full analytical sensitivities in NURBS based isogeometric shape optimization, Computer Methods in Applied Mechanics and Engineering 199 (2010) 2059–2071.

57. M. Scott, M. Borden, C. Verhoosel, T. Sederberg, T. J. R. Hughes, Isogeometric finite element data structures based on Bézier extraction of T-splines, International Journal for Numerical Methods in Engineering 88 (2011) 126 – 156.

58. E. Evans, M. Scott, X. Li, D. Thomas, Hierarchical t-splines: Analysis-suitability, Bézier extraction, and application as an adaptive basis for isogeometric analysis, Computer Methods in Applied Mechanics and Engineering 284 (2015) 1–20.

59. P. Hennig, S. Müller, M. Kästner. Bézier extraction and adaptive refinement of truncated hierarchical NURBS. Computer Methods in Applied Mechanics and Engineering 305 (2016) 316-339.

60. D. D'Angella, S. Kollmannsberger, E. Rank, A. Reali, Multi-level Bézier extraction for hierarchical local refinement of isogeometric analysis, Computer Methods in Applied Mechanics and Engineering 328 (2018) 147–174.

61. R. Balcaen, P.L. Reu, P. Lava, D. Debruyne, Stereo-DIC Uncertainty Quantification based on Simulated Images, Experimental Mechanics 57(6)939–951(2017)

62. R. Bouclier, J.-C. Passieux, M. Tirvaudey, L. Chamoin and M. Chapelier, Un pont global entre AIG et MEF : Calcul et optimisation de forme, isogéométrique, non-intrusif à partir d'un code EF industriel. Proceedings of CSMA 2019, Giens, France, 2019.

How to cite this article: G. Colantonio., M. Chapelier, R. Bouclier, J.-C. Passieux, and E. Marenić (2020), Non-invasive multilevel geometric regularization of mesh-based 3D shape measurement , *Int. J. Numer. Meth. Engrg.*, *10.1002/nme.6291*.